J. Mountain Res. P-ISSN: 0974-3030, E-ISSN: 2582-5011 DOI: https://doi.org/10.51220/jmr.v21-i1.30
Vol. 21(1), (2026) 292-302

# Magnetohydrodynamic Behavior of Unsteady Nanofluid Flow with Heat and Mass Transfer over Deforming Surfaces under Buoyancy Effects

**Ravindra Negi[1*] • Abhay Kumar[2]**

*[1]School of Humanities, Physical & Mahematical Sciences, Shobhit Institute of Engineering & Technology, Modipuram, Meerut 250110, India*
*[2]Department of Mathematics, Hemvati Nandan Bahuguna Garhwal University, Srinagar Garhwal, Uttarakhand 246174, India*

[*]Corresponding Author Email Id: rnegi7334@gmail.com

**Received: 27.04.2026.; Revised: 11.06.2026; Accepted: 11.06.2026**


**Abstract:** This research explores the unsteady magnetohydrodynamic (MHD) flow of a nanofluid over a stretching surface, with a focus on heat and mass transfer characteristics. The governing equations for fluid flow, heat transfer and mass concentration are transformed into ordinary differential equations through the application of similarity transformations. The analysis considers the influence of a transverse magnetic field along with thermal and solutal buoyancy forces and nanoparticle diffusion driven by thermophoresis and Brownian motion. Numerical simulations are implemented to evaluate the effect of critical parameters, including M, $P_r$, $S_c$ and nanoparticle buoyancy parameters ($N_t$ and $N_b$) on velocity, temperature and concentration distributions. The results illustrate that increasing the magnetic field intensity reduces velocity due to magnetic damping, while higher Prandtl numbers suppress the thermal boundary layer. Additionally, variations in $S_c$, $N_t$ and $N_b$ significantly impact concentration profiles. These findings provide practical insights for enhancing nanofluid-based heat and mass transfer applications in industries such as cooling systems and chemical processing.
**Key words:** MHD, unsteady flow, finite difference method, nanofluid, heat and mass transfer

**Nomenclature:**

| | |
|---|---|
| $u$ | velocity component in the X-direction (along the flow) |
| $v$ | velocity component in the y-direction (normal to the flow) |
| $U_w$ | stretching velocity |
| $X$ | longitudinal coordinate (along the stretching surface) |
| $Y$ | transverse coordinate (normal to the surface) |
| $T$ | time |
| $P$ | pressure field |
| $B_0$ | magnetic field strength |
| $Q$ | heat generation term (internal heat source) |
| $C_p$ | specific heat capacity at constant pressure |
| $T$ | temperature field |
| $T_w$ | stretching temperature |
| $T_\infty$ | ambient temperature (far-field temperature) |
| $C$ | concentration of nanoparticles |
| $C_w$ | stretching concentration |
| $C_\infty$ | ambient concentration (far-field concentration) |
| $D_B$ | diffusion coefficient |
| $S_c$ | schmidt number |
| $P_r$ | prandtl number |
| $R_d$ | Reynolds number |
| $E_c$ | Eckert number |
| $N_t$ | thermal buoyancy parameter |
| $N_b$ | solutal buoyancy parameter |
| $M$ | magnetic field parameter |
| $f(\eta)$ | dimensionless velocity profile |

**Greek symbols:**

| | |
|---|---|
| $P$ | density of the fluid |
| $N$ | kinematic viscosity of the fluid |
| $A$ | thermal diffusivity of the fluid |
| $\Sigma$ | electrical conductivity of the fluid |
| $H$ | similarity parameter |
| $\theta(\eta)$ | dimensionless temperature profile |
| $\varphi(\eta)$ | dimensionless concentration profile |
| $\lambda$ | stretching parameter of the surface |

## Introduction

Magnetohydrodynamic (MHD) flow is a subject of significant interest due to its relevance in numerous engineering and industrial applications, including cooling technologies, nuclear power plants and advanced energy systems. Recently, attention has shifted towards MHD flows involving nanofluids, which are mixtures of nanoparticles dispersed in conventional base fluids due to its ability to significantly improve the effectiveness and functionality of various thermal and fluid systems. These nanofluids exhibit superior thermal conductivity and enhanced transport properties, making them highly suitable for improving the efficiency of heat and mass transfer processes.

Radhika et al. (2025) highlighted the enhanced heat transfer, reduced velocity under magnetic fields, increased temperature from viscous dissipation and the impact of suction, slips and nanofluid properties on flow dynamics. Akter et al. (2025) have demonstrated that higher power-law index and Hartmann number reduce heat and mass transfer, emphasizing the influence of fluid properties and magnetic fields on non-Newtonian MHD convection. Pal (2025) have investigated the improved heat and mass transfer with increased ferroparticle volume, reduced temperature gradient from thermal radiation and enhanced mass transport due to higher Schmidt number in ferro-nanofluid flow. Zaheer et al. (2024) revealed that magnetic fields enhance mass transfer, buoyancy increases velocity, and higher Prandtl and Lewis numbers improve heat transfer, while stretching and convective parameters impact flow and temperature profiles. Akbar et al. (2024) showed in their study that buoyancy forces reduce skin friction, assisting flows enhance convection and increased fluid relaxation time slows flow and reduces cooling in Tangent Hyperbolic nanofluid over a stretchable plate. Razzaq and Farooq (2024) highlighted reduced velocity with increasing magnetic fields, enhanced thermal profiles from radiation and heat generation and increased Nusselt number with higher Prandtl number in hybrid nanofluid flow. Reddy et al. (2023) have investigated unsteady MHD mixed convection with porosity, radiation and viscous dissipation effects, showing their influence on heat and mass transfer. Results, validated via Keller–Box method, align well with previous findings. Ram Sharma and Jain (2024) explored in their study that buoyancy-driven nonlinear mixed convection in MHD flow, showing how stretching parameters, suction/injection and thermal buoyancy affect velocity, temperature, concentration and related industrial applications. Khan W. et al. (2024) have examined thermal and solutal transport in MHD flow through a porous vertical tube, highlighting suction influence and dual solutions, with significant applications in engineering processes. Khan M.S. et al. (2024) explored double diffusion convection of Casson fluids, revealing that higher Rayleigh numbers enhance convection and entropy, while increased buoyancy ratio and Darcy number improve heat/mass transfer and convection efficiency. Obalalu et al. (2024) have investigated magnetized two-phase nanofluid flow in solar thermal systems, showing enhanced heat transfer with increased nanoparticle volume fraction and electrical conductivity, using wavelet-based methods for solution. Eid et al. (2017) analyzed the effects of magnetic fields and heat generation on non-Newtonian nanofluid flow, showing increased thermal and concentration boundary-layer thickness with higher magnetic field and heat generation in pseudo-plastic nanofluids. Shateyi et al. (2017) examined Casson fluid flow, showing that magnetic parameter, Prandtl number and thermal radiation reduce velocity, temperature and heat transfer rate. Hamad and Pop (2011) analyzed unsteady MHD nanofluid flow past an oscillating vertical plate with heat source, using perturbation approximations to examine the effects of key physical parameters on

J. Mountain Res. P-ISSN: 0974-3030, E-ISSN: 2582-5011 DOI: https://doi.org/10.51220/jmr.v21-i1.30
Vol. 21(1), (2026) 292-302

flow behavior. Nadeem and Lee (2012) investigated nanofluid flow over an exponential stretching surface and the equations are simplified and solved using the homotopy analysis method (HAM), with results for velocity, temperature and nanoparticle volume fraction. Oliveira et al. (2011) explored viscoelastic fluid flow at the microscale, covering rheological properties, governing equations, passive mixing methods and microfluidic systems, emphasizing their industrial applications, cost-effectiveness and integration with electronics. Kandasamy et al. (2010) examined electrically conducting fluid flow, revealing that decreased viscosity reduces velocity, while thermophoresis affects the concentration boundary layer, with results discussed graphically.

This paper investigates unsteady MHD flow of a nanofluid over a stretching surface, analyzing heat and mass transfer under the influence of various parameters like magnetic field, buoyancy forces and nanoparticle diffusion to optimize nanofluid-based applications.

**Mathematical Formulation**

This study examines a single-phase nanofluid, comprising a base fluid (e.g. water, ethylene glycol or oil) and suspended nanoparticles, known for their favorable thermal and physical properties, it follows Buongiorno's two-component nanofluid model, in which nanoparticle transport due to Brownian motion and thermophoresis is explicitly considered. This is reflected in the governing energy and concentration equations through the inclusion of the Brownian motion parameter (Nb) and thermophoresis parameter (Nt).A two-dimensional system based on Cartesian coordinates is used, with the X-axis aligned along the stretching or shrinking surface and the Y-axis perpendicular, extending into the nanofluid. Surface temperature $(T_w > T_\infty)$ and concentration $(C_w > C_\infty)$ drive heat and mass transfer. The induced magnetic field is neglected under the assumption of a low magnetic Reynolds number. This assumption is commonly adopted in MHD flow analyses where the electrical conductivity of the fluid and the characteristic fluid velocity are sufficiently small, causing the induced magnetic effects to be negligible compared to the applied transverse magnetic field. The governing equations are derived from fundamental principles: the continuity equation for mass conservation, the Navier-Stokes equation for momentum with MHD effects and energy and concentration equations incorporating thermophoresis and Brownian motion. For completeness, their generalized forms in Cartesian coordinates are presented as follows:

Continuity Equation:

$$\frac{\partial u}{\partial x}+\frac{\partial v}{\partial y}=0 \qquad \dots (2.1)$$

Momentum Equation:

$$\frac{\partial u}{\partial t}+u\frac{\partial u}{\partial x}+v\frac{\partial u}{\partial y}=v\frac{\partial^2 u}{\partial y^2}-\sigma\frac{B_0^2 u}{\rho} \qquad \dots (2.2)$$

Energy Equation:

$$\frac{\partial T}{\partial t}+u\frac{\partial T}{\partial x}+v\frac{\partial T}{\partial y}=\alpha\frac{\partial^2 T}{\partial y^2}+\frac{Q}{\rho C_p} \qquad \dots (2.3)$$

Concentration Equation:

$$\frac{\partial C}{\partial t}+u\frac{\partial C}{\partial x}+v\frac{\partial C}{\partial y}=D_B\frac{\partial^2 C}{\partial y^2} \qquad \dots (2.4)$$

The initial constraints are described as follows:

$v=0\,,\ u=U_w(x,t),\ T=T_w(x,t),\ C=C_w(x,t) \quad at\ y=0$

$u\to 0,\ T\to T_\infty,\ C\to C_\infty\ as\ y\to\infty$ … (2.5)

Now, introduce the following non-dimensional variables

$\eta=\sqrt{\frac{a}{\nu(1+bt)}}\,y,\ u=axf'(\eta),\ v=-\sqrt{\frac{a\nu}{1+bt}}\,(f+\eta f'),\ M=\frac{\sigma B_0^2\nu}{\rho v_0^2},$

$\theta(\eta)=\frac{T-T_\infty}{T_w-T_\infty},\ \phi(\eta)=\frac{C-C_\infty}{C_w-C_\infty}$ … (2.6)

Substituting into the governing equations yields a system of dimensionless ODEs shown below:

$f'''+ff''-(f')^2-\eta f'=0$ … (2.7)

$\theta''+P_r(f\theta'-\lambda\theta)+E_c(f'')^2+R_d\theta'''=0$ … (2.8)

$\phi''+S_c(f\phi'-\lambda\phi)+N_t\theta''+N_b\phi''=0$ … (2.9)

In non-dimensional form, the equivalent initial boundary conditions are:

$f(0)=0,\ f'(0)=1,\ \theta(0)=1,\ \phi(0)=1\ \text{ when } \eta=0$

$f'(\eta)\to 0, \theta(\eta)\to 0,\ \phi(\eta)\to 0\ \text{as}\ \eta\to\infty$ … (2.10)

**Numerical Solution**

In this segment, we have discussed the solution of the set of governing irregular dimensionless partial differential equations, along with the corresponding primary and limiting parameters. The method of finite differences has been applied to determine solutions to equations (2.1)-(2.4) governed by the boundary conditions. A flow field in a rectangular region was chosen. This area is associated with both axes and divided into grid lines (Fig. 1). Both axes are orthogonal to each other and extend in their respective directions. Here, we have used $X_{max}(=125)$ and $Y_{max}(=50)$ in the same manner as the plate levels and $Y\to\infty$. The grid spacing numbers are m=150 and n=150 along the X and Y axes. With a smaller time step of $\Delta\tau=0.0005$, the constant grid dimensions are regarded as $\Delta X = 0.8$ and $\Delta Y = 0.2$ towards the X and Y axes. By applying the finite difference approach, we derived a suitable ensemble of finite difference equations from the partial differential equations (2.1) -(2.4).

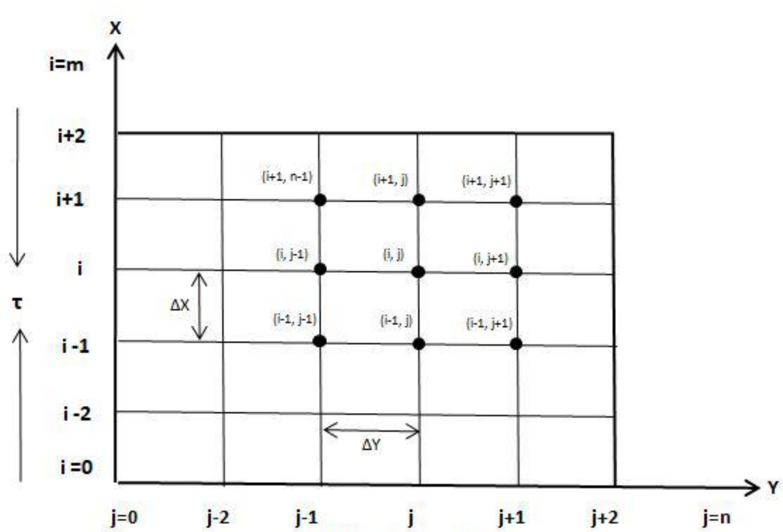


Fig. 1. Finite difference grid spacing

$$\frac{U_{ij}-U_{i-1j}}{\Delta X}+\frac{V_{ij}-V_{ij-1}}{\Delta Y}=0 \quad \ldots (3.1)$$

$$\frac{U'_{ij}-U_{ij}}{\Delta\tau}+U_{i,j}\left(\frac{U_{ij}-U_{i-1j}}{\Delta X}\right)+V_{i,j}\left(\frac{U_{i,j+1}-U_{ij}}{\Delta Y}\right)=\nu\left(\frac{U_{ij+1}-2U_{i,j}+U_{i,j-1}}{(\Delta Y)^2}\right)-\sigma\frac{B_0^2}{\rho} \quad \ldots (3.2)$$

$$\frac{T'_{ij}-T_{ij}}{\Delta\tau}+U_{ij}\left(\frac{T_{ij}-T_{i-1j}}{\Delta X}\right)+V_{ij}\left(\frac{T_{ij+1}-T_{ij}}{\Delta Y}\right)=\alpha\left(\frac{T_{ij+1}-2T_{ij}+T_{ij-1}}{(\Delta Y)^2}\right)+\frac{Q}{\rho C_p} \quad \ldots (3.3)$$

$$\frac{C'_{ij}-C_{ij}}{\Delta\tau}+U_{ij}\left(\frac{C_{ij}-C_{i-1j}}{\Delta X}\right)+V_{ij}\left(\frac{C_{ij+1}-C_{ij}}{\Delta Y}\right)=D_B\left(\frac{C_{ij+1}-2C_{ij}+C_{ij-1}}{(\Delta Y)^2}\right) \quad \ldots (3.4)$$

With boundary conditions:

$$V^n_{i,0}=0,\ U^n_{i,0}=U_w,\ T^n_{i,0}=T_w,\ C^n_{i,0}=C_w$$
$$U^n_{i,L}\to 0,\ T^n_{i,L}\to T_\infty,\ C^n_{i,L}\to C_\infty \quad as\ L\to\infty \quad \ldots (3.5)$$

Here, $\tau=n\Delta\tau$. Where n=integers denotes the time value.

## Results and Discussion

The results of the study which include temperature, velocity and concentration profiles for various parameter sets, are presented below.

As $P_r$ increases, the velocity decreases (Fig. 2) across all η, reflecting lower thermal diffusivity and momentum transfer, this causes a thinner velocity boundary layer. The velocity further diminishes with increasing η due to flow deceleration and the influence of $P_r$ intensifies at larger η.

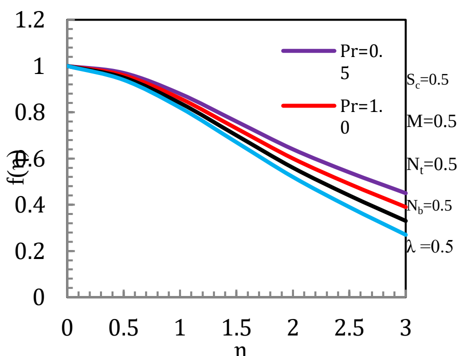


Fig. 2. velocity profile for distinct value of Pr

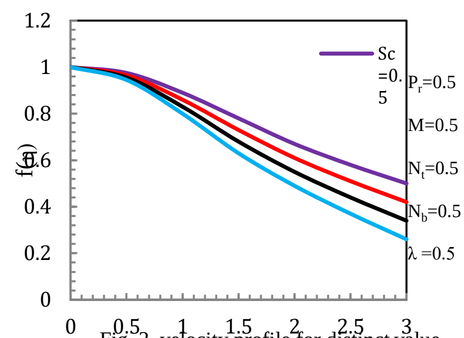


Fig. 3. velocity profile for distinct value of Sc

A increase in $S_c$ reduces velocity (Fig. 3) across all η, indicating decreased mass diffusivity and a thinner concentration boundary layer. Velocity continues to decrease with higher η and the reduction becomes more pronounced at larger η due to greater resistance to mass diffusion at higher $S_c$. Increasing the magnetic parameter reduces velocity (Fig. 4) due to magnetic damping, which opposes the flow. The velocity profile depends on η, reaching its maximum at the surface (normalized to 1.0) and decreasing with distance, indicating flow deceleration under the impact of the magnetic field.

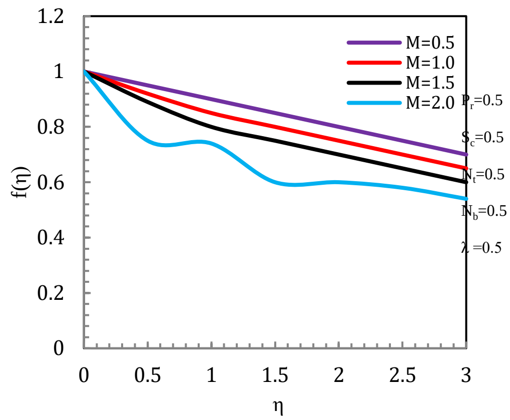

Fig. 4. velocity profile for distinct value of M

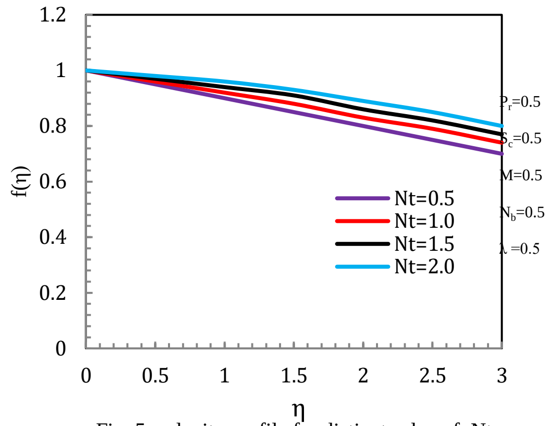

Fig. 5. velocity profile for distinct value of Nt

An increase in the thermal buoyancy parameter enhances velocity (Fig. 5) due to stronger buoyancy forces accelerating the flow. Velocity is greatest at the surface, where the stretching or shrinking effect is strongest and decreases with distance (η) as the flow progresses away from the surface.

With an increase in the solutal buoyancy parameter, velocity increases (Fig. 6) due to enhanced buoyant forces from concentration gradients, which accelerate the flow. As typical in boundary layer flow, the velocity is maximal at the surface and decreases as the distance (η) from the surface increases.

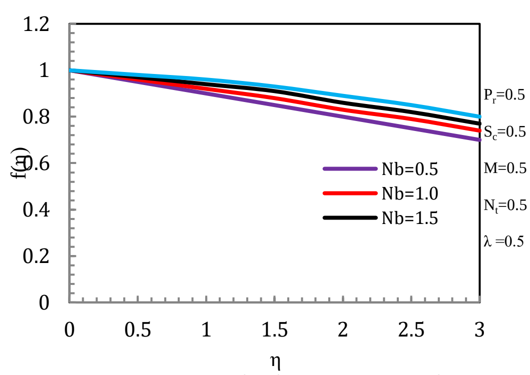

Fig. 6. velocity profile for distinct value of Nb

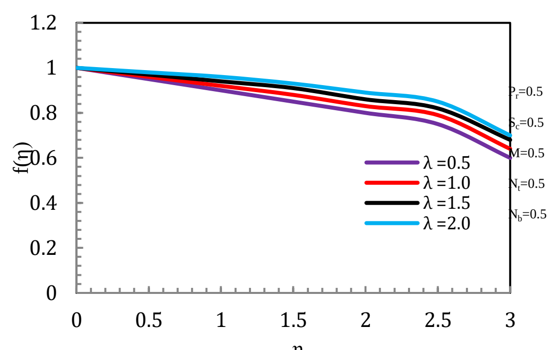

Fig. 7. velocity profile for distinct values of λ

For a stretching surface (λ>0), velocity increases (Fig. 7) with λ as the surface accelerates the flow, with higher velocities at λ=2.0 compared to λ=0.5. Velocity is greatest at the surface and decreases with increasing η. As the Prandtl number increases, the temperature near the surface decreases (Fig. 8) more quickly due to a thinner thermal boundary layer, leading to a steeper temperature gradient. For lower $P_r$, the boundary layer is thicker, resulting in a more gradual temperature change. Temperature is highest at the surface and decreases with increasing η.

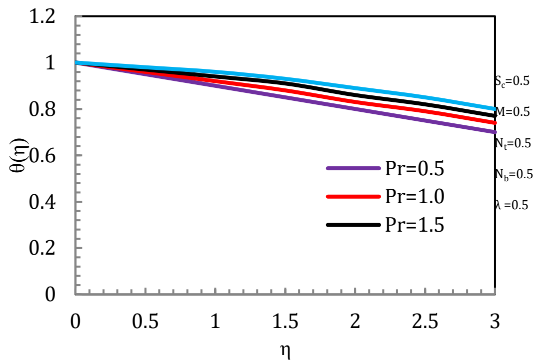

Fig. 8. temperature profile for distinct value of Pr

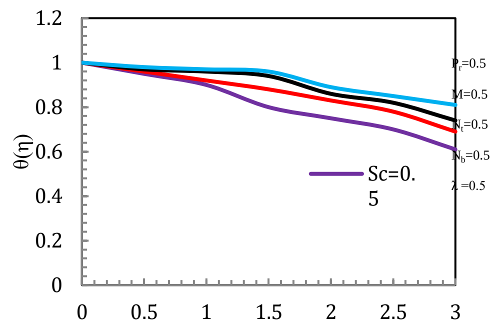

Fig. 9. temperature profile for distinct value of Sc

As the Schmidt number increases, the concentration boundary layer thins, which decrease the temperature (Fig. 9) gradient near the surface as mass transfer slows, and thermal diffusion becomes more dominant. Temperature is highest at the surface and decreases with increasing η, consistent with boundary layer flow behavior.

With a rise in the magnetic parameter, velocity decreases (Fig. 10) due to magnetic damping, which causes the thermal boundary layer to thin and steepens the temperature gradient near the surface, resulting in lower overall temperatures. Temperature is highest at the surface and decreases with increasing η, as typical in boundary layer flow.

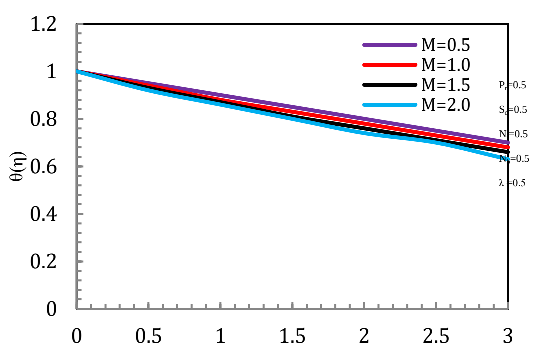

Fig. 10. temperature profile for distinct value of M

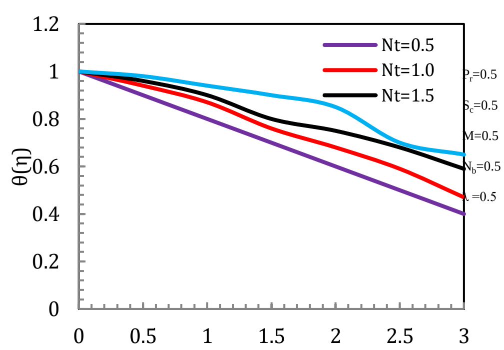

Fig. 11. temperature profile for distinct value of Nt

As the thermal buoyancy parameter increases, temperature near the surface increases (Fig. 11) due to enhanced buoyant forces, leading to a thicker thermal boundary layer and higher surface temperatures. Temperature is highest at the surface and decreases with increasing η, with a steeper gradient near the surface that gradually flattens outward.

As the solutal buoyancy parameter increases, solutal buoyancy effects strengthen, leading to a thicker concentration (Fig. 12) boundary layer and potentially higher surface temperatures due to improved heat transfer. Temperature is highest at the surface and decreases with increasing η, with a steeper gradient near the surface.

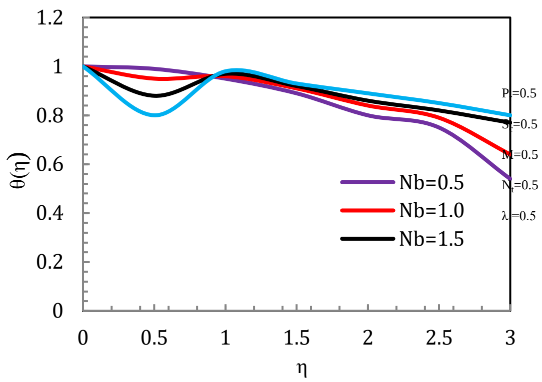


Fig. 12. temperature profile for distinct value of Nb

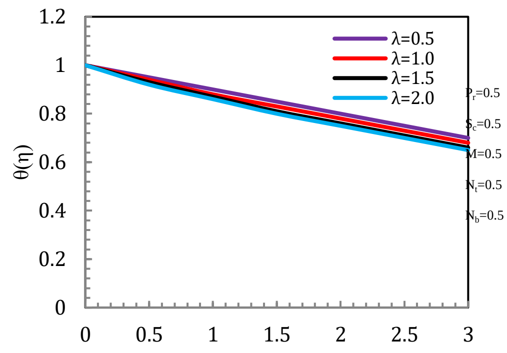


Fig. 13. temperature profile for distinct values of λ

As the stretching parameter (λ) increases, the surface stretches more quickly, leading to a thinner thermal boundary layer and lower temperatures (Fig. 13) snear the surface. Temperature is highest at the surface and decreases with increasing η, with a steeper gradient near the surface that gradually flattens outward. As $P_r$ increases, thermal diffusivity decreases (Fig. 14), influencing concentration distribution. Higher $P_r$ values result in a thinner concentration boundary layer and reduced concentration farther from the surface. Concentration is highest at the surface and decreases with increasing η, with a more significant reduction at higher $P_r$.

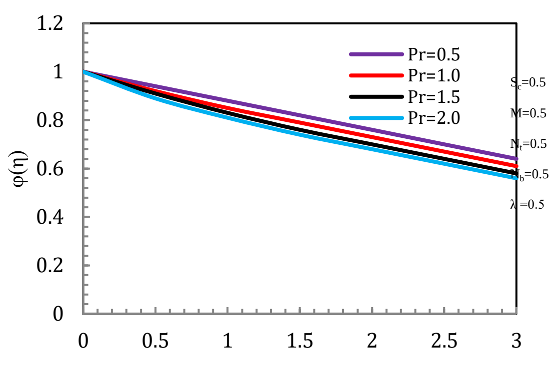


Fig. 14. concentrartion profile for distinct value of Pr

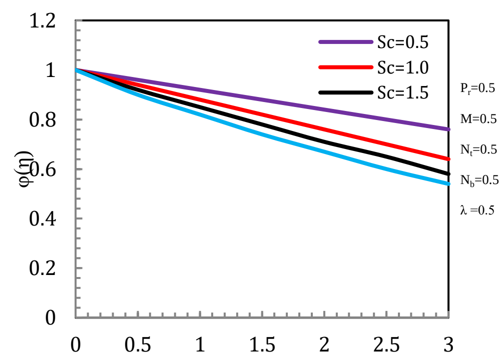


Fig. 15. concentration profile for distinct value of Sc

As $S_c$ increases, mass diffusivity decreases (Fig. 15), resulting in a thinner concentration boundary layer and a faster decrease in concentration with increasing η. Concentration is highest at the surface and decreases with η, with a more gradual decline at lower Sc, indicating a thicker boundary layer. An increase in the M weakens convective transport (Fig. 16), causing a thicker concentration boundary layer and higher concentration further from the surface. Lower M enhances convection, thinning the boundary layer and lowering concentration at greater η. Concentration decreases with increasing η, with a more gradual decline at higher M.

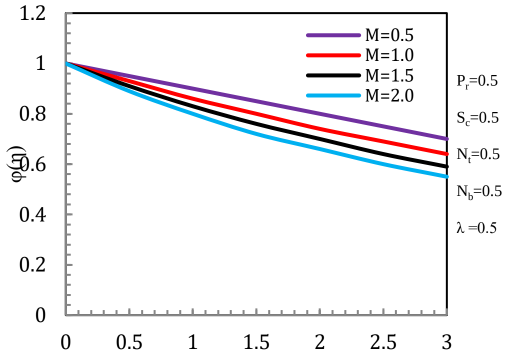

Fig. 16. concentration profile for distinct value of M

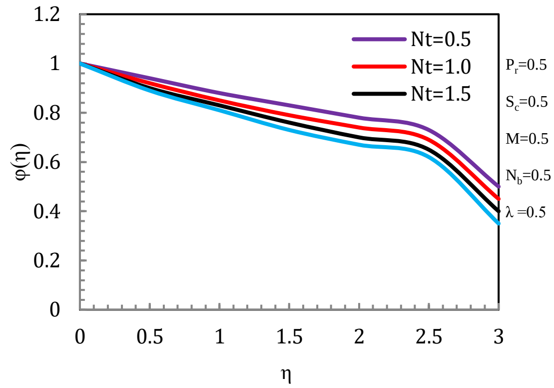

Fig. 17. concentration profile for distinct value of Nt

An increase in $N_t$ intensifies buoyancy effects, resulting in a thicker concentration boundary layer (Fig. 17) and higher concentration further from the surface. Lower $N_t$ leads to a thinner boundary layer with steeper concentration gradients. Concentration decreases with increasing η, with a more gradual decline at higher $N_t$. An increase in $N_b$ enhances buoyancy effects, resulting in a thicker concentration boundary layer and a slower decrease (Fig. 18) in concentration with increasing η. Lower $N_b$ leads to a thinner boundary layer with steeper concentration gradients. Concentration decreases with η, decaying more gradually at higher $N_b$.

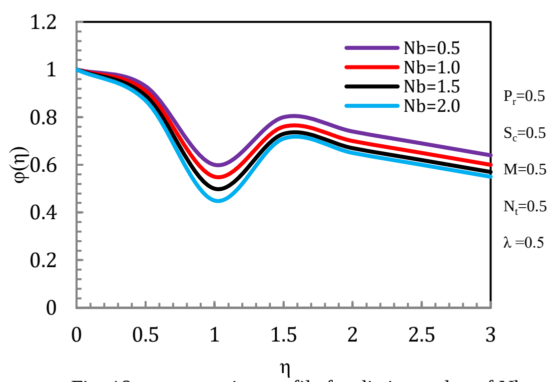

Fig. 18. concentration profile for distinct value of Nb

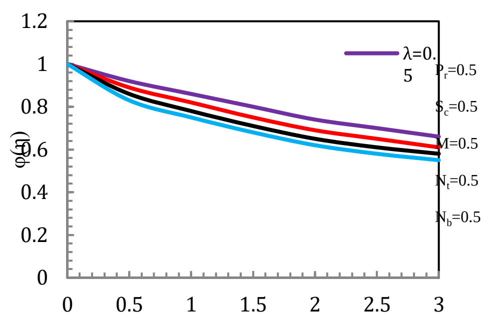

Fig. 19. concentration profile for distinct value of λ

In stretching conditions (λ>0), the concentration boundary layer becomes thinner, leading to a faster decrease in concentration (Fig. 19) with increasing η. Higher λ accelerates the concentration drop due to increased transport from surface stretching.

**Conclusion**

We have examined the equations (1) – (4) for the flow of a single-phase nanofluid and suspended nanoparticles along the boundary conditions. The consequence of different parameters $P_r$ , $S_c$ , $N_t$ , $N_b$ , M and λ are studied in detail. We have solved our dimensionless equations by employing a finite difference method. The findings are deliberated for varying parameter values. The key findings of the study are summarized below:

(i) The results indicate that parameters such as Pr, Sc, M, $N_t$ and $N_b$ significantly influence the velocity and concentration profiles of the nanofluid flow. Higher values of $P_r$ and $S_c$ reduce the velocity and thin the momentum boundary layer, whereas increasing M, Nt and Nb enhances the fluid velocity. Moreover, the stretching surface parameter ($\lambda>0$) accelerates the flow near the surface. These findings are practically important in the design of advanced thermal systems, polymer extrusion processes, cooling devices and coating technologies, where controlling fluid motion and transport characteristics is essential for improving heat and mass transfer efficiency.

(ii) The study further reveals that increasing the $P_r$ and $S_c$ decreases the thermal boundary layer thickness and reduces the surface temperature, while larger values of M, $N_t$ and $N_b$ increase the temperature distribution due to enhanced thermal boundary layer growth. The stretching surface parameter also contributes to lower surface temperatures through flow acceleration. These thermal characteristics provide useful insights for industrial and engineering applications involving nanofluid-based heat exchangers, electronic cooling systems, solar energy devices and thermal management technologies where precise temperature regulation is required.

(iii) The concentration analysis demonstrates that higher values of $P_r$, $S_c$ and M suppress concentration distribution, whereas increasing $N_t$, $N_b$ and $\lambda$ thickens the concentration boundary layer and slows concentration decay away from the surface. The concentration remains maximum near the surface and gradually decreases with increasing $\eta$. These observations are valuable for applications involving chemical processing, biomedical transport, drying technologies and material manufacturing, where accurate control of nanoparticle concentration and mass transfer behavior plays a crucial role in enhancing process performance and product quality.

**Reference**

Akbar N S, Noor T, Muhammad T & Alghamdi M (2024). Thermal analysis of non-Newtonian ferro nanofluid flow due to stretching surface under buoyancy effects through numerical computation. *Numerical Heat Transfer, Part B: Fundamentals*, 1–15.

Akter S, Akter H, Islam M M & Molla M M (2025). Magnetohydrodynamic natural convection and sensitivity analysis of heat and mass transfer of non-Newtonian fluid in concentric cylinders with wall heat and mass flux. *Multiscale and Multidisciplinary Modeling, Experiments and Design*, *8*(1), 55.

Eid M R & Mahny K L (2017). Unsteady MHD heat and mass transfer of a non-Newtonian nanofluid flow of a two-phase model over a permeable stretching wall with heat generation/absorption. *Advanced Powder Technology*, *28*(11), 3063-3073.

Hamad MAA, Pop I (2011). Unsteady MHD free convection flow past a vertical permeable flat plate in a rotating frame of reference with constant heat source in a nanofluid. *Heat Mass Transfer* **47**, 1517–1524.

Kandasamy R, Muhaimin I (2010). Scaling Transformation for the Effect of Temperature-Dependent Fluid Viscosity with Thermophoresis Particle Deposition on MHD-Free Convective Heat and Mass Transfer Over a Porous Stretching Surface. *Transp Porous Med* **84**, 549–568

Khan M S, Ahmad S, Shah Z, Alshehri A, Vrinceanu N & Garalleh H A (2024). Computational study of double diffusive MHD natural convection flow of non-Newtonian fluid between concentric cylinders. *Results in Engineering*, *21*, 101925.

Khan W, Saidani T, Smarandache F, Khan M S, Ayed H & Abdou M M M (2024). Two-dimensional steady squeezing flow over a vertical porous channel with free convective heat/mass transfer and invariable suction. *Case Studies in Thermal Engineering*, *60*, 104800.

Nadeem Sand Lee C (2012).. Boundary layer flow of nanofluid over an exponentially stretching surface. *Nanoscale Res Lett* **7**, 94 (2012).

Obalalu AM, Oni MO, Khan U *et al*.(2024) . Two-Phase Numerical Simulation for the Heat and Mass Transfer Evaluation Across a Vertical Deformable Sheet with Significant Impact of Solar Radiation and Heat Source/Sink. *Arab J Sci Eng* **49**, 11053–11071

Oliveira M S, Alves M A & Pinho F T (2011). Microfluidic flows of viscoelastic fluids. *Transport and Mixing in Laminar Flows: From Microfluidics to Oceanic Currents*, 131-174.

Pal D (2025). Impact of Arrhenius activation energy on thin film flow in nonlinearly thermally radiative kerosene-based ferro-nanofluid with aligned magnetic field. *International Journal of Ambient Energy*, *46*(1).

Radhika M & Reddy Y D (2025). Viscous dissipation and radiation effects on MHD heat transfer copper water nanofluid flow over an exponentially shrinking surface. *Multiscale and Multidisciplinary Modeling, Experiments and Design*, *8*(2), 132.

Ram Sharma K & Jain S (2024). A numerical study of MHD nonlinear mixed convection flow over a nonlinear vertical stretching sheet with the buoyancy and suction/injection effects. *Numerical Heat Transfer, Part B: Fundamentals*, 1–30.

Razzaq R & Farooq U (2024). Non-similar analysis of MHD hybrid nanofluid flow over an exponentially stretching/shrinking sheet with the influences of thermal radiation and viscous dissipation. *Numerical Heat Transfer, Part B: Fundamentals*, 1–16.

Reddy Y D, Goud B S, Nalivela N R & Rao V S (2023). Impact of porosity on two-dimensional unsteady MHD boundary layer heat and mass transfer stagnation point flow with radiation and viscous dissipation. *Numerical Heat Transfer, Part A: Applications*, *85*(8), 1172–1190.

Shateyi S, Mabood . & Lorenzini G (2017). Casson fluid flow: Free convective heat and mass transfer over an unsteady permeable stretching surface considering viscous dissipation. *J. Engin. Thermophys.* **26**, 39–52

Zaheer M, Abbas S Z, Huang N & Elmasry Y (2024). Analysis of buoyancy features on magneto hydrodynamic stagnation point flow of nanofluid using homotopy analysis method. *International Journal of Heat and Mass Transfer*, *221*, 125045.